Natural Product Reports

Structure-based engineering of α-ketoglutarate dependent oxygenases in fungal meroterpenoid biosynthesis

Journal:	*Natural Product Reports*
Manuscript ID	NP-REV-02-2022-000014.R1
Article Type:	Review Article
Date Submitted by the Author:	09-May-2022
Complete List of Authors:	Awakawa, Takayoshi; The University of Tokyo, Graduate School of Pharmaceutical Sciences Mori, Takahiro; The University of Tokyo Ushimaru, Richiro; The University of Tokyo, Graduate School of Pharmaceutical Sciences Abe, Ikuro; The University of Tokyo, Graduate School of Pharmaceutical Sciences

ARTICLE

Structure-based engineering of α-ketoglutarate dependent oxygenases in fungal meroterpenoid biosynthesis

Received 00th January 20xx,
Accepted 00th January 20xx

DOI: 10.1039/x0xx00000x

Takayoshi Awakawa[a,b]*, Takahiro Mori[a,b,c], Richiro Ushimaru[a,b,d], Ikuro Abe[a,b]*

Covering: Up to February 2022

Non-heme iron- and α-ketoglutarate-dependent oxygenases (αKG OXs) are key enzymes that play a major role in diversifying the structures of fungal meroterpenoids. They activate a specific C-H bond of the substrate to first generate a radical species, which is usually followed by oxygen rebound to produce cannonical hydroxylated products. However, in some cases remarkable chemistries induce dramatic structural changes in molecular scaffolds, depending on the stereoelectronic characters of the substrate/intermediates and the resulting conformational changes/movements of the active site of the enzyme. Their molecular bases have been extensively investigated by crystallographic structural analyses and structure-based mutagenesis, which revealed intimate structural details of the enzyme reactions. This information facilitates the manipulation of the enzyme reactions to create unnatural, novel molecules for drug discovery. This review summarizes recent progress in the structure-based engineering of the αKG OX enzymes, involved in the biosynthesis of polyketide-derived fungal meroterpenoids. The literature published from 2016 through February 2022 will be reviewed.

1 Introduction

Meroterpenoids are defined as a group of hybrid natural products that consist of non-terpenoid and terpenoid moieties. The fungal meroterpenoids mainly possess polyketide-derived skeletons, although they occasionally include molecular scaffolds derived from other biosynthetic origins, as in the indole and shikimate-derived meroterpenoids.[1] The enzymes responsible for fungal meroterpenoid biosynthesis have been well characterized,[2] and the information regarding their structures and functions has been utilized to create structurally diverse, unnatural novel meroterpenoids through engineered biosynthesis.[3-5] This review mainly focuses on the work toward the discovery, structural analysis, and protein engineering of the enzymes involved in the biosynthesis of polyketide-derived fungal meroterpenoids.

The biosynthesis of polyketide-derived meroterpenoids is achieved by polyketide synthases (PKSs), prenyltransferases (PTs), flavin-dependent monooxygenases (FMOs), terpene cyclases (CYCs),[6] and tailoring enzymes, including isomerases, transferases, and oxidases, such as cytochrome P450 oxygenases (P450s)[7] or non-heme iron- and α-ketoglutarate-

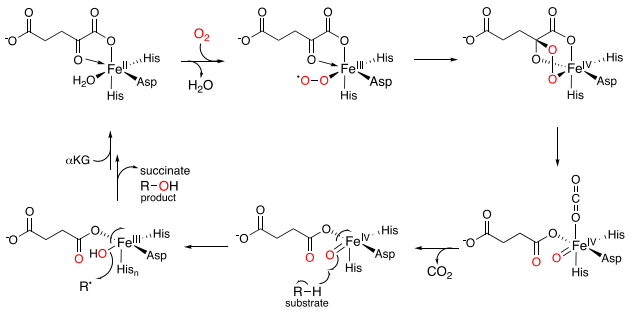

Figure 1. The general catalytic cycle for non-heme iron- and α-ketoglutarate-dependent oxygenase.

[a] Graduate School of Pharmaceutical Sciences, The University of Tokyo, Bunkyo-ku, Tokyo 113-0033, Japan
[b] Collaborative Research Institute for Innovative Microbiology, The University of Tokyo, Yayoi 1-1-1, Bunkyo-ku, Tokyo 113-8657, Japan
[c] PRESTO, Japan Science and Technology Agency, Kawaguchi, Saitama, Japan.
[d] ACT-X, Japan Science and Technology Agency, Kawaguchi, Saitama, Japan

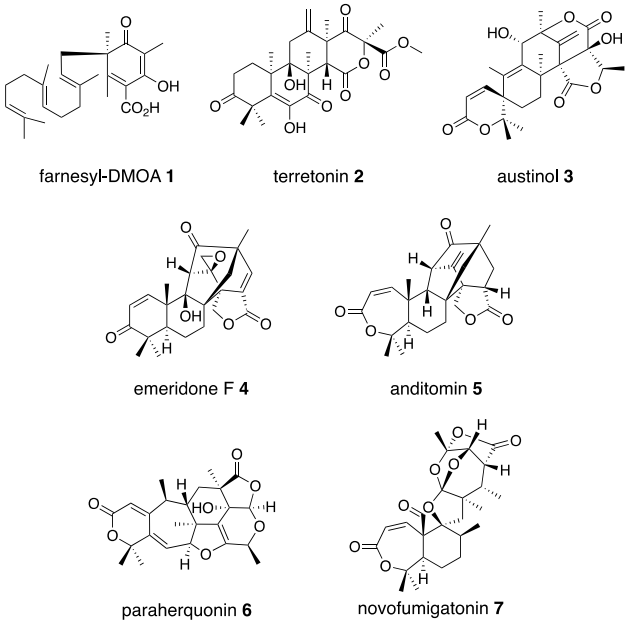

Figure 2. Fungal meroterpenoids derived from farnesyl-DMOA 1.

dependent oxygenases (αKG OXs).[2,8-11] PKS constructs polyketide core from acetate-derived building blocks, PT installs prenyl side-chain, FMO oxidizes the olefin of the prenyl group to form an epoxide, and CYC catalyzes protonation-initiated cyclization of the terpene moiety, and the tailoring enzyme decorates the resultant scaffold to generate the complex structures of meroterpenoids. Among the tailoring enzymes, αKG OXs often play a crucial role in amplifying the structural diversity and complexity of the molecules.[12-17] They employ mononuclear non-heme Fe(II) and the co-substrate αKG, and generate a highly reactive ferryl-oxo intermediate (Fe(IV)=O) with the concomitant oxidative decarboxylation of αKG to succinate.[18,19] The Fe(IV)=O first abstracts a hydrogen atom from a specific unactivated C-H bond in the substrate (Fig. 1). The generated intermediate radical species facilitates a wide range of reactions, including hydroxylation, desaturation, epoxidation, C-X bond formation, and C-C bond reconstruction.[2,3,5,8-10,12-21] As a result, diverse meroterpenoid structures are produced, as exemplified by the biosyntheses of farnesyl-3,5-dimethylorsellinic acid (DMOA) **1** derived terretonin **2**, austinol **3**, emeridone F **4**, anditomin **5**, paraherquonin **6**, and novofumigatonin **7** (Fig. 2).[2] The structural basis of the αKG OX enzyme reactions has recently been extensively studied by X-ray crystallography and site-directed mutagenesis experiments. In this review, the recent progress in the structure-based engineering of the αKG OX enzymes to create unnatural novel molecules for drug discovery will be summarized.

2 AusE/PrhA in Austinol/Paraherquonin Biosynthesis

AusE and PrhA are multifunctional αKG OX enzymes that accept the common substrate preaustinoid A1 **8**, but catalyze different regioselective dehydrogenations to produce preaustinoid A2 **9** in austinol **3** biosynthesis in *Aspergillus nidulans* and

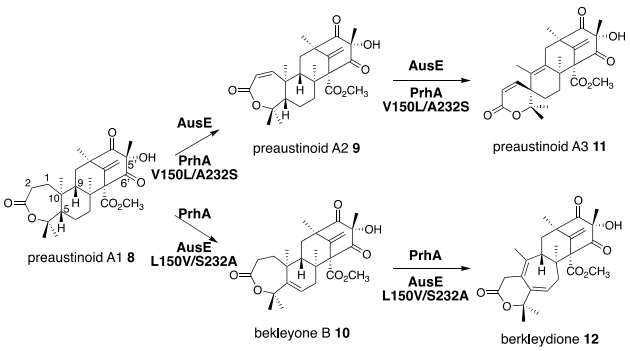

Figure 3. Syntheses of preaustinoid A3 11 and berkleydione 12 from the common substrate preaustinoid A1 8 by AusE and PrhA. PrhA-V150L/A232S catalyzes the AusE reaction to produce **11**, and AusE-L150V/S232A catalyzes the PrhA reaction to produce **12**.

berkeleyone B **10** in paraherquonin **6** biosynthesis in *Penicillium brasilianum*, respectively (Fig. 3).[22,23] AusE further catalyzes spirolactone ring formation to produce preaustinoid A3 **11**, while PrhA catalyzes cycloheptadiene formation to produce berkeleydione **12**. Because AusE and PrhA share high amino acid sequence identity (78%), the two homologous enzymes are excellent models for a comparative analysis to investigate the underlying differences in the catalytic mechanisms of meroterpenoid diversification. The X-ray crystal structures of AusE/PrhA were reported as the first examples of the αKG OXs in fungal meroterpenoid biosynthesis.[24] While AusE was crystallized in complex with Mn(II), which does not serve as a functional cofactor for the oxygenation, PrhA was crystallized with Fe(II) in its active site under anaerobic conditions. The overall structures of AusE/PrhA are symmetric homodimers consisting of a double-stranded β-helixes (DSBH) core, a.k.a. jelly-roll, cupin, or jumonji C fold, which includes the residues for substrate binding and the 2-H-1-D (H130-D132-H214) triad for metal-binding (Fig. 4a).[12] The analysis of PrhA complexed with Fe, αKG, and **8** (PrhA-Fe/αKG/**8**) provided important information regarding the manner of substrate binding (Fig. 4b). Remarkably, the structural analyses revealed significant conformational changes upon substrate binding. The Cα of the S66 Loop A in Chain B moves 5.4 Å toward the active site, to interact with D276' and the 5'-OH and 6'-carbonyl of **8**. The newly generated hydrogen bonding fixes Hairpin B, which is only detected when the protein is complexed with **8**. Upon acceptance by the enzyme, the conformation of the A-ring of **8** is altered from a chair to boat conformation. The A/B-rings of **8** are surrounded by three hydrophobic residues V150, A232, and M241, and one hydrophilic residue N152 (Fig. 4b). In contrast, the D-ring of **8** interacts with several hydrophilic residues, including R72 at the β-sheet, N127 and R128 at Loop C, and D276' in Hairpin B, as well as Loop A 57-69 and Hairpin 267'-280' (from another monomer). The region including these residues was proposed to function as a lid for substrate binding. The 6'-carbonyl of **8** is hydrogen bonded with the C-1

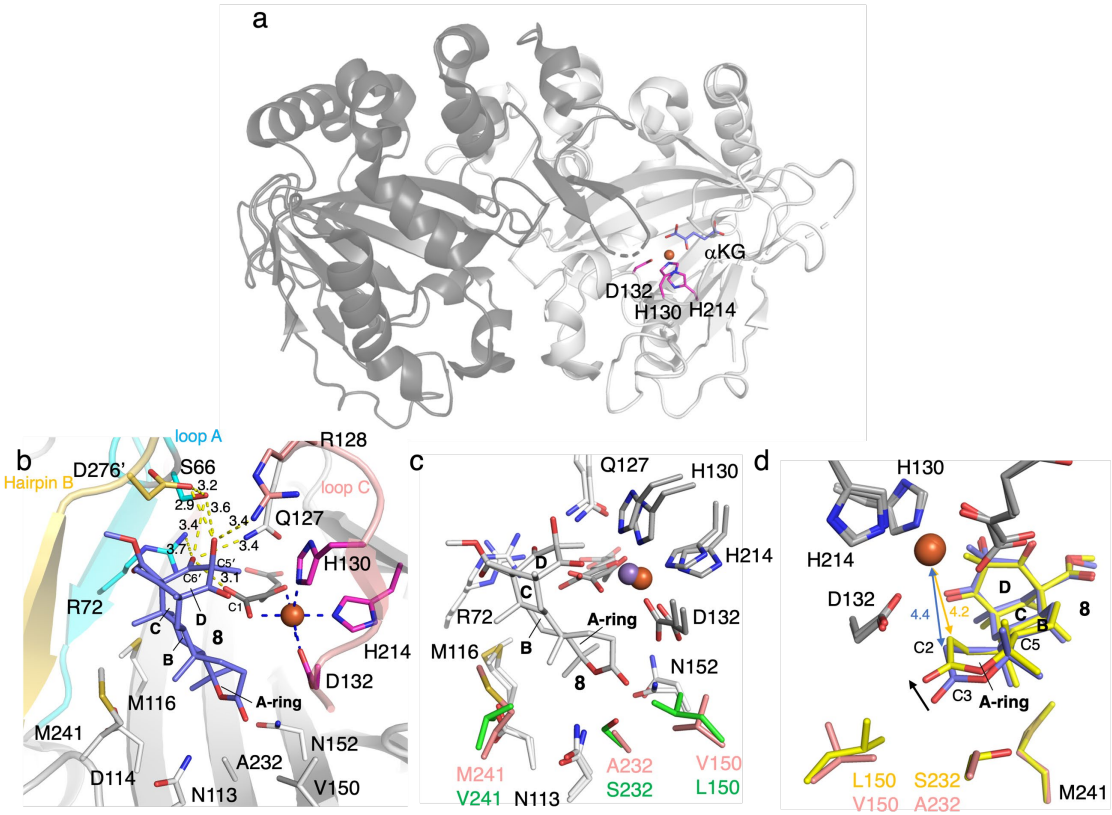

Figure 4. Structures of AusE and PrhA. (a) The overall structure of PrhA (PDBID: 5YBN). αKG and catalytic triad residues are shown in blue and magenta sticks, respectively. (b) Active site structure of PrhA-Fe/αKG/**8** (PDBID: 5YBO). Loop A and loop C in Chain B are represented with cyan and salmon cartoon, respectively. The hairpin loop from adjoining monomer is depicted in yellow cartoon. **8** and αKG are shown as blue and grey sticks, respectively. (c) Comparison of the active site residues between the AusE and PrhA structures (PDBID: 5YBL and 5YBO). PrhA and AusE are represented by salmon- and green-colored residues, respectively. **8** and αKG are shown as white and grey sticks, respectively. (d) Comparison of binding modes of **8** in PrhA wild type (salmon, PDBID: 5YBO) and PrhA-V150L/A232S (yellow, PDBID: 5YBP). **8** in PrhA wild type, **8** in PrhA-V150L/A232S, and αKG are shown as blue, yellow, and grey sticks, respectively. Yellow dashed lines show hydrogen bond interactions. Blue dashed lines represent coordination of metal atom. Orange and purple spheres show iron and manganese atoms, respectively. The key distance between iron atom and carbon atoms are shown as arrows. The units of distances are Å. The oxygen, nitrogen, and sulfur atoms are colored red, blue, and yellow, respectively.

carboxylate of αKG, suggesting the requirement of αKG for substrate binding.

The comparison of the AusE and PrhA structures revealed that V150, A232, and M241 in PrhA are replaced with L150, S232, and V241 in AusE (Fig. 4c). To evaluate the effects of these substitutions, these three amino acid pairs were replaced with their counterpart residues. Remarkably, the AusE S232A variant produced **12** and **11** in comparable amounts, and AusE L150V/S232A produced **12** as a major product. As anticipated, the PrhA V150L/A232S variant produced **11** as a major product. The k_{cat} and K_m values of AusE L150V/S232A and PrhA V150L/A232S were very similar to those of PrhA and AusE, respectively, indicating that they efficiently catalyze the non-native reactions. Thus, the structure-based engineering successfully achieved the functional interconversion of the two enzymes. The crystal structures of PrhA-V150L/A232S and PrhA-V150L/A232S/M241V complexed with each substrate revealed that the position of the D-ring of the substrate does not change, because it is tightly fixed by Loop A and Hairpin B, while significant conformational changes shift the orientation of the A/B rings toward the iron center (Fig. 4d). The wild-type PrhA abstracts H-5 of **8**, leading to the production of **10**, while PrhA V150L/A232S abstracts H-2 to produce **9**, as in the case of wild-type AusE (Fig. 3). Based on the altered regioselectivities, it is likely that the A-ring of **8** undergoes a boat-to-chair flip and the C-2 of the substrate becomes closer to the iron in PrhA V150L/A232S than that in the wild-type enzyme (4.2 Å vs 4.4 Å). This example shows how the enzyme active site dictates the conformation of the terpene moiety of the substrate, leading to the two different regioselectivities of the reactions. In PrhA

V150L/A232S complexed with **9**, the distance between H-5 and Fe(II) is the shortest, which is consistent with the proposed mechanism of the reaction initiation by the abstraction of H-5. After the formation of **9**, the reconstruction of the spirocycle ring system is proposed as follows. The C-5 radical first reacts with the double bond between C-1 and C-2, resulting in the cyclopropylcarbinyl radical intermediate, and the C-2 radical then reacts with an electron of the bond between C-1 and C-10, followed by the dehydrogenation of H-9 and the formation of the C-9/C-10 double bond, to produce **11** (Fig. 5a).

Interestingly, the PrhA V150L/A232S variant oxidizes C-13 of **11** to produce unnatural novel products, **13** and **14**, and PrhA V150L/A232S/M241V further oxidizes **13** into **16,** and **14** into **15** (Fig. 5b). The crystal structure of PrhA V150L/A232A with **11** revealed that the C-10/C-13 bond is rotated clockwise by 30° , thus reducing the distance from C-13 to Fe(II).

It is remarkable that the double amino acid substitutions V150L and A232S in PrhA increase the number of oxidations from two (**8** to **11**) to five times (**8** to **16**). Because the structure of the D-ring of the substrate does not change during the reaction, the enzyme can recognize and accommodate the oxidized products **9**, **11**, **13**, and **14**, even though its A/B ring structures are altered significantly. The prediction and evaluation of the conformational changes of substrates in the active site of the enzyme are crucial to rationally design the structures of molecules, as illustrated in the *in silico*-designed targeted protein engineering of class I terpene cyclases.[25,26]

3 AndA in Anditomin Biosynthesis

AndA, another multifunctional αKG OX active during anditomin **5** biosynthesis, desaturates the bond between C-1 and C-2 of preandiloid B **17** to produce preandiloid C **18**, and also catalyzes the subsequent isomerization (not oxidation!) to yield andiconin **19** through a dynamic skeletal rearrangement (Fig. 6).[27] The X-ray crystallographic analysis and density functional theory (DFT) calculations of the reaction intermediates were conducted to clarify its catalytic mechanism.[28] The apo structure of AndA exhibits the conserved DSBH fold with a funnel-like reaction chamber (Fig. 7a),[12,24] and the complex structures with **17** or **18** revealed that the substrates are bound to the interface of the two monomers, in similar manners to

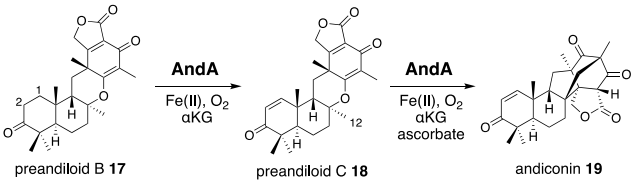

Figure 6. Andiconin 19 synthesis from preandiloid B 17 by AndA.

AusE and PrhA (Figs. 7bc). Loop A (Loop 58-76, between α2 and β3) from one monomer and Loop B' (Loop 261'-281', between α7' and α8') from the other monomer, and R239 located at the Loop structure, constitute a lid for the active site. Loop A is not visible in the apo-structure, and in the complex structure, it is bound to the D/E rings of the substrate. The two carbonyl oxygen atoms O-3 and O-5 of **17** are anchored to a water molecule (w1) supported by the side chain of Y272' and the main chains of N67 and I70, and O-4 is bound to two water molecules (w2 and w3) coordinated by the side chain of E66 and the main chains of K63 and N67 (Fig. 7b). The terpenoid moiety (the A/B/C rings) of **17** is mainly supported by hydrophobic interactions, except for one hydrogen bonding between O-1 and N121. Since a water molecule (w4) and the carboxylic oxygen of αKG (O-2/αKG) are considered to occupy the identical positions to the oxo species of Fe(IV)=O, the distances from each carbon atom of the substrate to w4 or O-2/αKG were compared. As a result, the calculated distances were 4.4 Å (C-1 to w4), 4.0 Å (C-2 to w4), 3.3 Å (C-1 to O-2/αKG), and 3.7 Å (C-2 to O-2/αKG), indicating that both H-1 and H-2 are sufficiently close enough for the hydrogen atom abstraction (Fig. 7b). The exact mechanism of the desaturation remains unclear even with the crystal structures, although three pathways can be proposed as shown in the mechanistic study of desaturation by AsqJ αKG OX in the viridicatin-type alkaloid biosynthetic pathway.[29]

In the isomerization reaction, which starts with the abstraction of H-12 of **18** which bound to an enzyme via O-1, -3, -4, and O-5 like **17**, the two distances from H-12 to O-2/αKG (3.5 Å) and to w4 (4.9 Å) support that the structure is reasonable for H-12 abstraction (Figs. 6, 7c). To further investigate the dynamics of the isomerization, the DFT calculation was

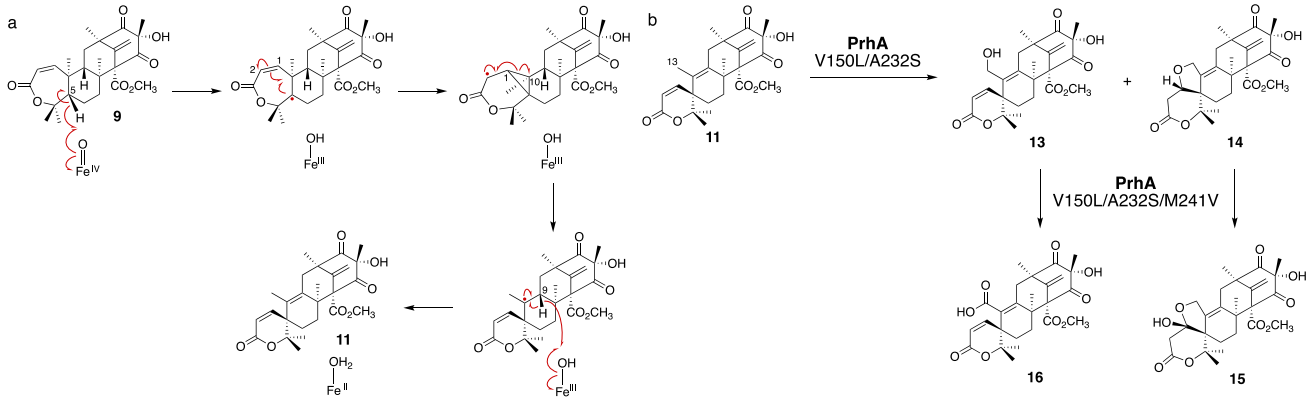

Figure 5. Proposed reaction mechanisms of AusE and PrhA V150L/A232S to synthesize 11 from 9 (a), and the reactions of PrhA V150L/A232S and V150L/A232S/M241V to synthesize 13 and 14, and 15 and 16, respectively (b).

performed.[28] After the H-12 abstraction of **18** to generate **18a**, four reaction steps can be proposed (Fig. 8): i) C8-O2 bond cleavage (**18a** to **18b**), ii) C12-C5′ bond formation (**18b** to **18c**), iii) C8-C2′ bond formation (**18c** to **18d**), and iv) quench of the C-7′ radical by ascorbic acid (**18d** to **19**). In accordance with the prediction that the energetically stable tertiary carbon radical **18b** is preferred, the calculated energy for the C-O bond cleavage is only 6.6 kcal/mol. In another pathway, anti-Baldwin 5-end-trig cyclization proceeds to yield the α-oxy carbon radical intermediate **18b'** with an activation energy of 23.4 kcal/mol, indicating that the pathway to **18b** is more likely than this pathway. During the conversion from **18c** to **18d**, several conformational changes with minute activation barriers are expected to occur, and the C-8 radical approaches to the Michael acceptor carbon center C-2′. The radical at C-7′ in **18d** is finally quenched by a reducing agent, resulting in the generation of **19**.

To examine the roles of the amino acids in the active site of AndA, N121, R239, and Y272′ were substituted with alanine or apolar residues with similar bulkiness. The AndA N121A variant exhibited reduced activity, and the AndA R239A, R239M, R239V, and Y272A variants only yielded **18** and failed to produce **19**. Because R239 and Y272′ interact with the lid-like Loop region, these substitutions likely interrupted the sequential conformational changes required for the isomerization reaction. These observations indicated the importance of the lid region to maintain the reaction.

The combination of structural and computational studies nicely illustrated the mechanism of the isomerization enzyme reaction to produce the unique bicyclo[2.2.2]octane system. Like AusE and PrhA,[24] AndA recognizes the A/B rings of **17** and **18** by hydrogen bonding with N121 and hydrophobic interactions, but not tight interactions as seen in those with the D ring, thus allowing the dynamic conformational changes of the intermediates during the enzyme reaction. Computational analyses of the enzyme-bound reaction intermediates will provide important information regarding how the enzyme manages the conformational changes of the substrate/intermediates. For example, the underlying reasons for the requirement of ascorbate in the *in vitro* enzyme reaction, the native reductant, and the mechanism of the reduction from **18d** to **19** remain unknown. Similar reductive radical quenching is also observed in several unique αKG OX enzyme reactions, including FtmOx1 (endoperoxidase),[30-32] CarC (epimerase),[33] and SnoN (epimerase),[34] but the mechanisms of their reductions remain obscure, even though they are essential for the functional conversions of αKG OXs from oxygenases to isomerases.

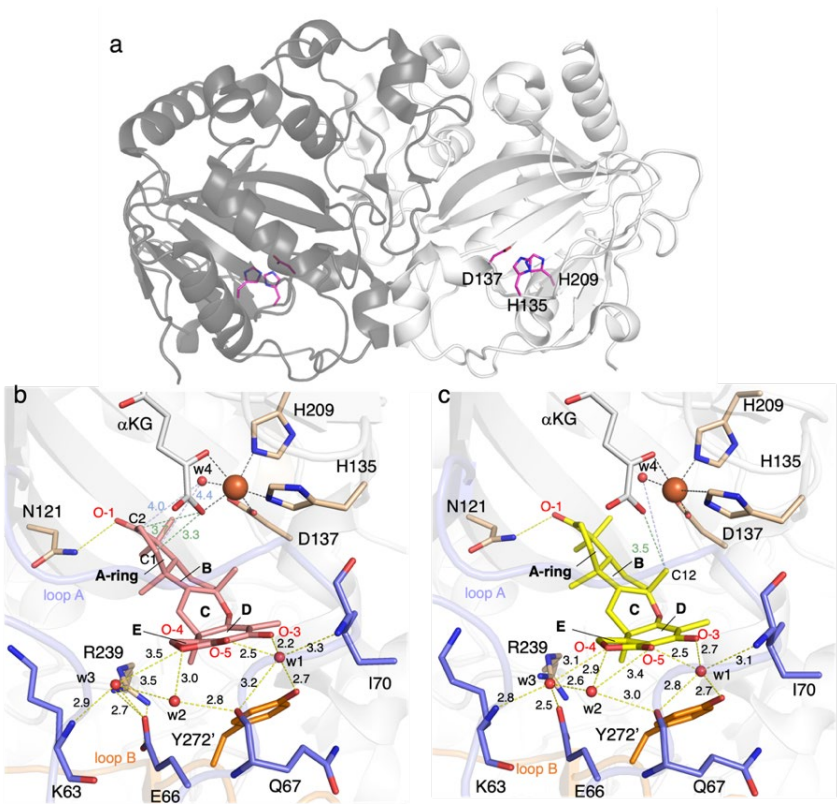

Figure 7. Structure of AndA. (a) The overall structure of AndA (PDBID: 5ZM2). The catalytic triad residues are shown in magenta sticks. (b) The active site architecture of AndA-Fe/αKG/**17** (PDBID: 5ZM3). **17** and αKG are represented as salmon and white sticks, respectively. (c) The active site architecture of AndA-Fe/αKG/**18** (PDBID: 5ZM4). **18** and αKG are represented as yellow and white sticks, respectively. Loop A and Loop B are colored blue and orange, respectively. Yellow dashed lines show hydrogen bond interactions. Black dashed lines represent coordination of metal atom. The orange spheres show iron atoms. The units of distances are Å. The oxygen and nitrogen atoms are colored red and blue, respectively. Red spheres show water molecules.The iron atoms are depicted by orange spheres. The units of distances are Å.

ARTICLE

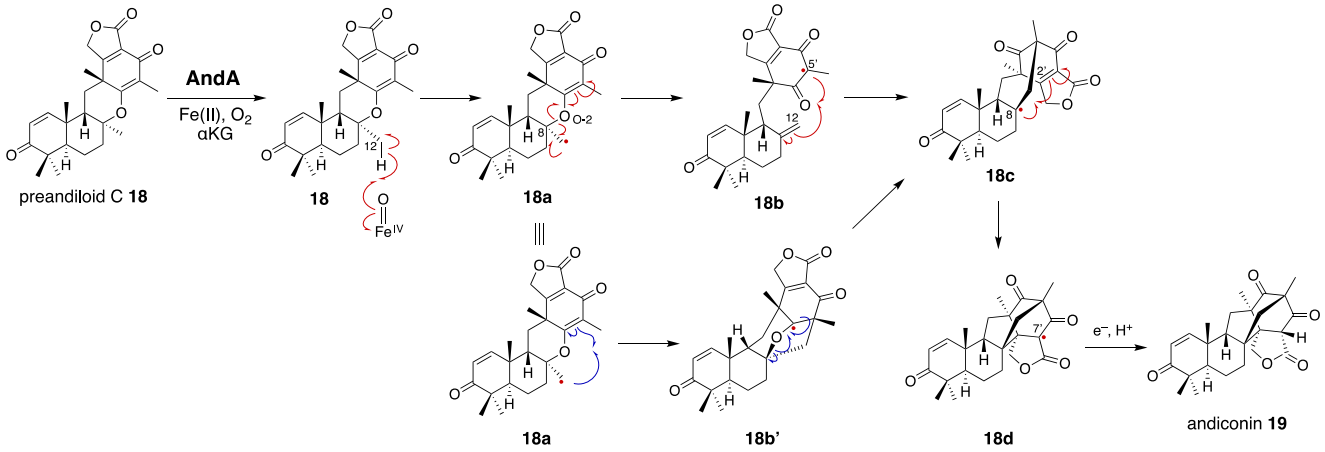

Figure 8. Proposed reaction mechanism of AndA to synthesize andiconin 19 from preandiloid C 18.

4 NvfI in Novofumigatonin Biosynthesis

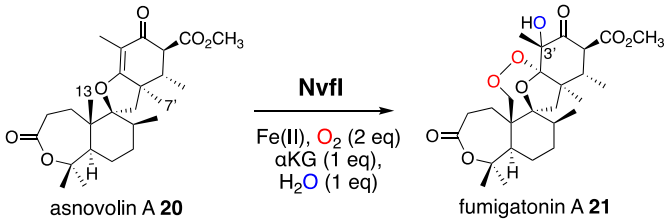

Figure 9. Synthesis of fumigatonin A 21 from asnovolin A 20 by NvfI.

Another remarkable αKG OX is NvfI, which installs the peroxide bridge on asnovolin A **20** to produce fumigatonoid A **21** in novofumigatonin **7** biosynthesis (Fig. 9).[35] The quantification of αKG and oxygen consumptions during the reaction suggested that one turnover of the NvfI reaction requires one equivalent of αKG and two equivalents of molecular oxygen.[36] Labeling experiments using $^{18}O_2$ and $H_2{}^{18}O$ indicated that two oxygen atoms at the endoperoxide moiety are derived from one molecular oxygen, and the one oxygen atom at the 3'-OH is derived from $H_2{}^{18}O$ (Fig. 9). The gel filtration analysis revealed that NvfI is the first monomeric αKG OX found in fungal meroterpenoid biosynthesis, similarly to the αKG OXs in the biosyntheses of other secondary metabolites, such as deacetoxycephalosporin C synthase.[37,38] Given that the previously described AusE/PrhA and AndA utilize the interface of the two monomers for substrate accommodation, the substrate binding manner of NvfI was expected to be different. The X-ray crystal structural analysis revealed that NvfI also adopts the DSBH fold, and its β1 and β3 strands unusually form a small β-barrel-like structure with three anti-parallel β-sheets (β4', β5', and β7') (Fig. 10a). The comparison of the apo- and complex- structures revealed that S122-G128 on Loop I and W199-P209 on Loop II undergo large conformational changes, when the substrate **20** is bound (Fig. 10b). As the Loop I alters its orientation toward the active site, F127 approaches to the catalytic center along with the movement of W199. The side chain of R201 also changes its orientation, and newly interacts with Y116 and D206 via water molecules. E208 also moves and forms a new hydrogen bond with K205, thus increasing the cavity volume of the DSBH fold.

Notably, the distance from C-7' of **20** to Fe(II) (4.2 Å) is shorter than the distance from C-13 (6.5 Å) in the complex structure (Fig. 10c), suggesting that this binding model is an artifact or represents the reaction of C-7' oxidation reaction to produce the derailment product **22** (Fig. 11). The docking

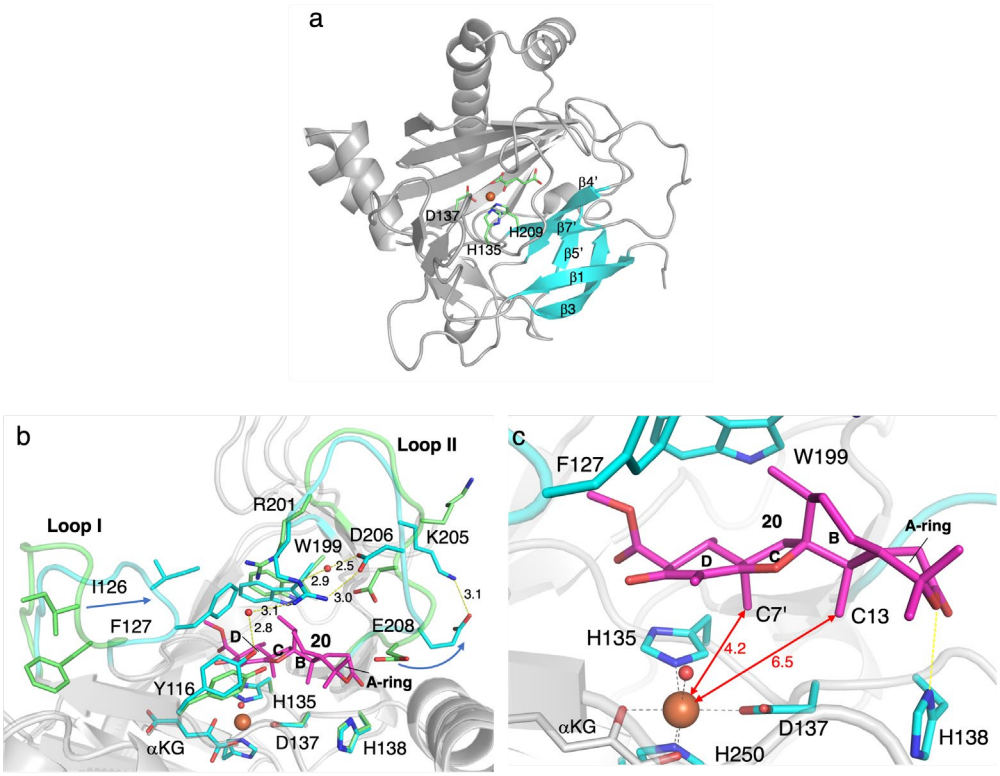

Figure 10. Structure of NvfI. (a) The overall structure of NvfI. The catalytic triad residues and αKG are shown in green sticks. The DSBH fold and the smaller β-barrel fold are colored gray and cyan, respectively. (b) Comparison of the active site structures of NvfI apo (PDBID: 7ENB) and NvfI-Fe/αKG/**20** (PDBID: 7DE2). **20** and αKG are shown as magenta and cyan sticks, respectively. Loop regions in apo and complex structures are colored green and cyan, respectively. Direction of the conformational changes of the loop regions are indicated by blue arrows. (c) Close-up view of the active site of NvfI-Fe/αKG/**20** (PDBID: 7DE2). **20** and αKG are shown as magenta and white sticks, respectively. Yellow dashed lines show hydrogen bond interactions. Black dashed lines represent the coordination of the metal atom. The key distances between the iron atom and carbon atoms are shown as arrows. The units of distances are Å. The oxygen and nitrogen atoms are colored red and blue, respectively. Red spheres show water molecules.

simulation of the NvfI-αKG binary complex with **20** indicated that the enzyme accommodates **20** by adjusting its conformation so that C-13 is located closer to Fe(II) than C-7′. Furthermore, the comparison of the NvfI-αKG and NvfI-αKG/**20** complex structures suggested that the movement of the Loop around E208 increases the volume of the enzyme active site around the A-ring of **20**, and the radical formation at C-13 and the following conformational changes move the substrate location deeper inside the tunnel (Fig. 10b).

The substitutions of F127 on Loop A and W199 on Loop B lead to the loss of activity, which showed that these residues are essential for the endoperoxide forming activity. Their roles were proposed as gate-keepers that retain the correct conformation of **20**. In other endoperoxide-forming enzymes; *i.e.*, heme-dependent prostaglandin H synthase (PGHS, also known as cyclooxygenase, COX)[39] and αKG OX fumitremorgin B endoperoxidase (FtmOx1),[30-32] the active site tyrosine residue close to the Fe(IV)=O was proposed to play a critical role to relay a radical from the reaction intermediate (Fig. 12). However, the substitution of the Y residues in the NvfI active site to F did not affect the reactivity. These data indicated that NvfI employs a distinct mechanism from those of PGHS and FtmOx1. Interestingly, NvfI H138A reduced the endoperoxide-forming activity by 20%, but newly generated **23** (Fig. 11), which indicated that the hydrogen bonding between H138 and the C-3 ester group is important to adjust the location of the substrate (Fig. 10c). Consequently, the reaction mechanism from **20** to **21** was proposed, as shown in Fig. 11. The Fe(IV)=O species abstracts the hydrogen atom from C-13 to generate the primary radical A, which reacts with O_2 to form the peroxide radical B. The generated radical B reacts with C-2′ to yield radical C, which then reacts with the Fe(III)-hydroxyl species to produce **21** (path a). It is also possible that electron transfer from the radical C to the ferric iron species generates the cationic intermediate D, and the successive attack by water yields **21** (path b). In path a, the oxygen ligands in the Fe(IV) and Fe(III) states should be exchanged with the solvent water during the catalysis as reported in the reaction of other αKG OX.[40] NvfI thus consumes only one molecule of αKG to produce one molecule of **21**, as hypothesized in the reaction mechanism described above. The absolute configuration of OH-3′ is restricted to the *R*-configuration, indicating that the enzyme controls the orientation of the hydroxyl-rebound or the addition of water.

The structural analysis of NvfI revealed how the monomeric αKG OX accepts the substrate with the conformational changes of Loop I and II. More importantly, this study proposed a new mechanism of the rare enzymatic endoperoxide formation reaction without the help of the tyrosine residue for the radical relay, although the possibility that other residues may work in the relay cannot be excluded. NvfI may suppress the direct

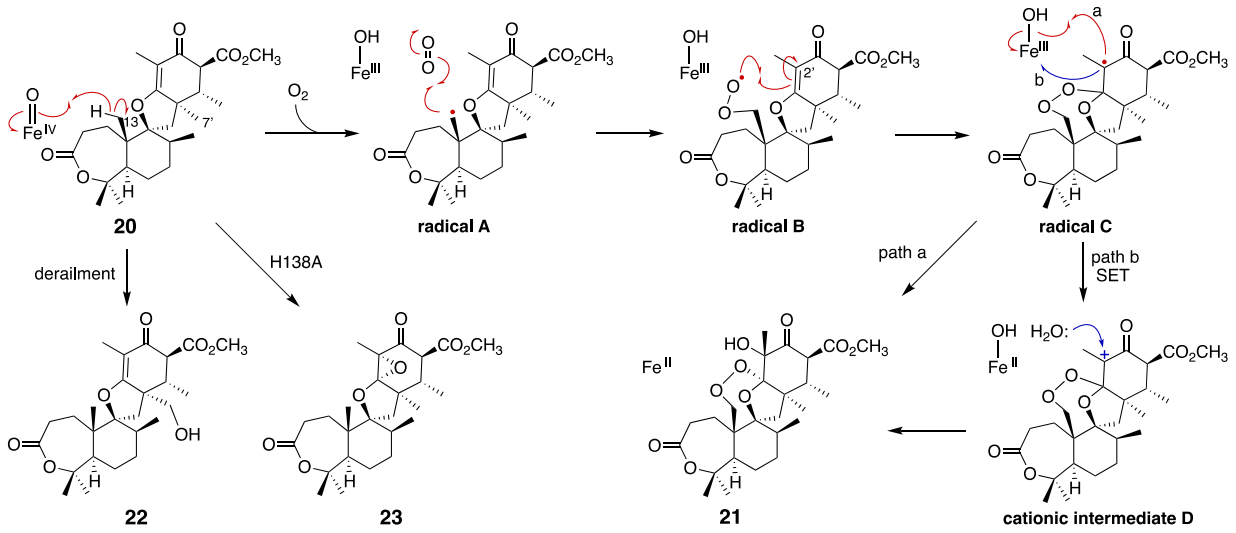

Figure 11. Proposed reaction mechanism of NvfI to synthesize 21 from 20. The structures of the derailment products **22** and the product **23** from the H138A variant reaction are also depicted.

oxygen rebound between the radical A and Fe(III)-OH by facilitating the large conformational changes of the radical A. The prolonged lifetime of the radical intermediates may lead to the reaction with molecular oxygen, although the mechanism of molecular oxygen retention in the enzyme remains enigmatic. This hypothesis of oxygen rebound prevention could be applicable to other non-hydroxylating αKG OX enzyme reactions.[12-16] This study provided useful information for future enzyme engineering to introduce unique chemical scaffolds into the products.

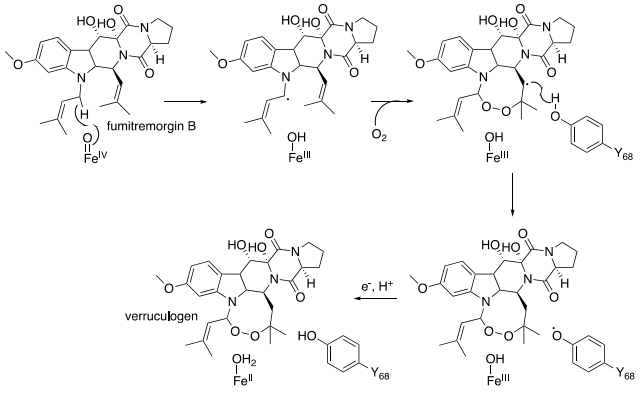

Figure 12. The reaction mechanism of FtmOx1 to synthesize verruculogen from fumitremorgin B.

5 TlxI-J in Talaromyolides Biosynthesis

Four αKG OXs, TlxA, C, I, and J, were identified in the biosynthesis of 6/6/6/6/6/6 hexacyclic meroterpenoids, talaromyolides **24a**-**f** and **25** (Fig. 13).[41,42] Their functions were analyzed by *in vitro* assays with **26** as a substrate, which showed that TlxJ oxidizes C-9α of **26** to yield **27**, but all TlxA, C, I, and J were inactive toward **27** when assayed individually.[43] The bioinformatic analysis indicated that TlxI lacks an arginine residue for αKG binding,[12] and the Loop As of TlxI and TlxC are

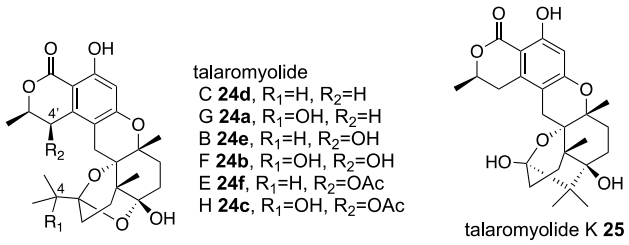

Figure 13. Chemical structures of talaromyolides 24a-f, 25.

shorter than those of other fungal αKG OXs. These analyses suggested that TlxI and TlxC lack the oxygenase functions and play auxiliary roles. In fact, the reaction with TlxI-J consumed **27** to produce talaromyolide G **24a**, talaromyolide C **24d**, talaromyolide K **25**, novel compounds **28**, and **29** (Figs. 13 and 14). The 4,5-secodriman products **24a**, **24d**, **28**, and **29** were generated by a retro-aldol reaction from the *trans*-drimane intermediate, and the hemiketal product **25** was produced in the reaction between the 9α-OH and 3-keto groups in the *cis*-drimane intermediate (Fig. 14a). Similarly, TlxA-C work together to hydroxylate **24a** and **24d** to produce **24b** and **24e**, respectively.

The reaction pathway from **27** to **24a**, **24d**, and **25** was proposed, as described below. First, TlxI-J abstracts H-5 to give the C-5a hydroxylated *trans*-drimane intermediate (Fig. 14a). The deprotonation of the OH-5a leads to the retro-aldol reaction which cleaves the C4–C5 bond, as proposed in yaminterritrem B biosynthesis,[44] and the resultant intermediate undergoes successive ketal formation to produce **24d**. The hydroxylation at C-4 of the retro-aldol reaction product generates **24a**. It is intriguing that **25** is derived from the *cis*-drimane intermediate, while its yield is lower than those of the other products. After radical formation at C-5, the *trans*-drimane is likely transformed into *cis*-drimane before the oxygen rebound.

Interestingly, the unnatural meroterpenoids **27** and **28** were also observed in the TlxI-J reaction (Fig. 14b). They are expected

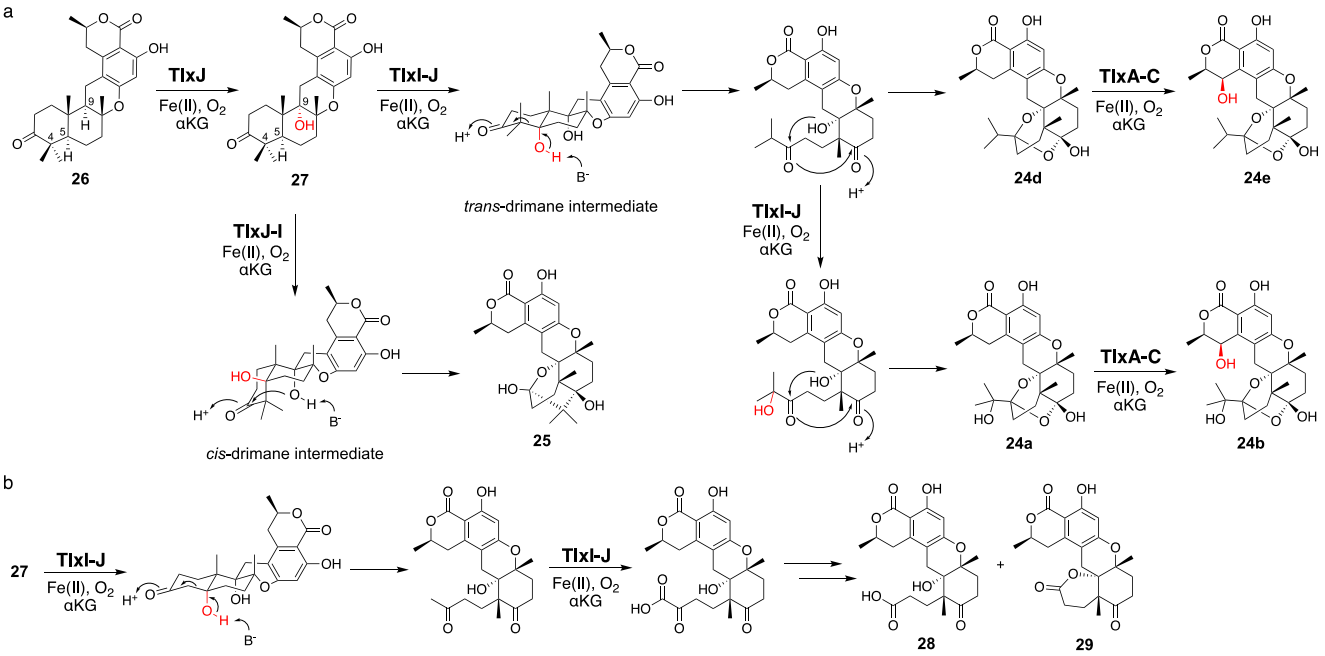

Figure 14. Reactions of monomer TlxJ and heterodimer TlxI-J to synthesize talaromyolides 24a, 24b, 24d, 24e, and 25 and unnatural analogs 28 and 29.

to be generated via repeated demethylations of C-14 and C-15 through sequential oxygenation from the methyl group to the carboxylic acid followed by decarboxylation, as in cholesterol biosynthesis[45] and terpenoid secondary metabolite biosynthesis.[46,47] The successive C-3 demethylation possibly proceeds via oxidative decarboxylation, as in αKG[18,19] and 4-hydroxyphenylpyruvate decarboxylation.[48,49]

The gel filtration analyses of TlxI-J and TlxA-C revealed that they form unprecedented αKG OX enzyme heterodimers.[12,13] The amounts of TlxJ and TlxA purified from an *Escherichia coli* expression system are low when they are solely expressed, but they are efficiently produced as a monomer or heterodimer when co-expressed with TlxI or TlxC. Together, these data indicated that TlxI and TlxC serve as chaperone-like proteins to increase the stability of TlxJ and TlxA, respectively. Interestingly, TlxC cannot be substituted for TlxI, and vice versa, indicating the rigid specificity for the heterodimer formation.

To investigate the molecular basis of the unprecedented αKG OX heterodimer, the X-ray crystal structure of TlxI-J complexed with Fe/N-oxalglycine (NOG)[50] was analyzed.[43] TlxJ in the heterodimer adopts the conserved DSBH fold, while TlxI does not possess a complete DSBH fold. In fact, Loop A' in TlxI is much shorter than the corresponding region of TlxJ (Fig. 15a). These observations suggest that the reaction chamber cannot be constructed in the TlxI monomer. Thus, in analogy with the other homodimeric αKG OXs such as PrhA and AndA,[11,16] a funnel-like substrate binding site is expected to be constructed with the DSBH fold (TlxJ) as a chamber, and Loop A (TlxJ) and Loop B' (TlxI) as a lid. The metal binding site (H136, D138, and H213) and αKG binding site (R224, N133, and T173) are conserved in the TlxJ structure, but the residue corresponding to R224 of TlxJ is substituted with S211 in TlxI (Fig. 15bc), indicating that TlxI cannot bind αKG.

The substitutions of the amino acid residues oriented toward the active site of TlxJ, including R120 and L239 located on the DSBH core and I259' located on Loop B', significantly reduced the reactivity, while these variants maintained the heterodimer structure as confirmed by gel filtration, suggesting that these residues are required for the substrate binding. Interestingly, TlxJL239A-I newly accumulated the C-1 hydroxylated **27**, indicating that the substitutions in the hydrophobic reaction chamber are effective to alter the reaction profile, as observed in PrhA/AusE and AndA.[24,28]

To investigate the differences between the heterodimer and homodimer structures, the amino acid residues located at the interface of TlxI-J were substituted. There are several amino acid pairs responsible for the hydrogen bonding, including R63' and S276, T224' and F236 (main chain), R135' and D152, and W262' and P238 (Fig. 16a). As expected, the TlxI R63'A, T224'A, R135'A, and W262'A variants no longer formed a heterodimer with TlxJ, as evidenced by pull-down assays, indicating that they are important for the interaction between the monomers. Comparisons of the structure of TlxI-J with those of PrhA and AndA demonstrated that the manner of heterodimer formation is quite different from that of homodimer formation (Fig. 16bc).

The reason why TlxJ requires TlxI to form a functional heterodimer remains to be elucidated. Since TlxJ exists as a monomer when it is produced in *E. coli*, it is likely that TlxJ cannot form a homodimer by itself. The TlxJ monomer can oxidize **26**, although this reaction is much slower than that of TlxI-J. These results indicated that the TlxJ monomer can also form a premature reaction cavity, but it requires TlxI to form a complete reaction cavity that can accept **27**. The CRISPR-based gene inactivation of *tlxI* abolished the production of talaromyolides and accumulated **27**, implying that TlxI-J also forms a heterodimer *in vivo*. This study presented the

characterization of the first heterodimeric αKG OXs. The interaction of each monomer in the heterodimer is quite different from that in the homodimer. Given that TlxI-J can catalyze a high number of oxygenations (possibly 11 times to synthesize **28** and **29**), the heterodimer structure might decrease the rigidity of substrate recognition. If two αKG OXs are artificially complexed as a heterodimer, a multifunctional heterodimer like TlxI-J could be created. The simulation showing the creation of the *cis*-drimane intermediate in the enzyme after the C-5 radical intermediate would also be intriguing.

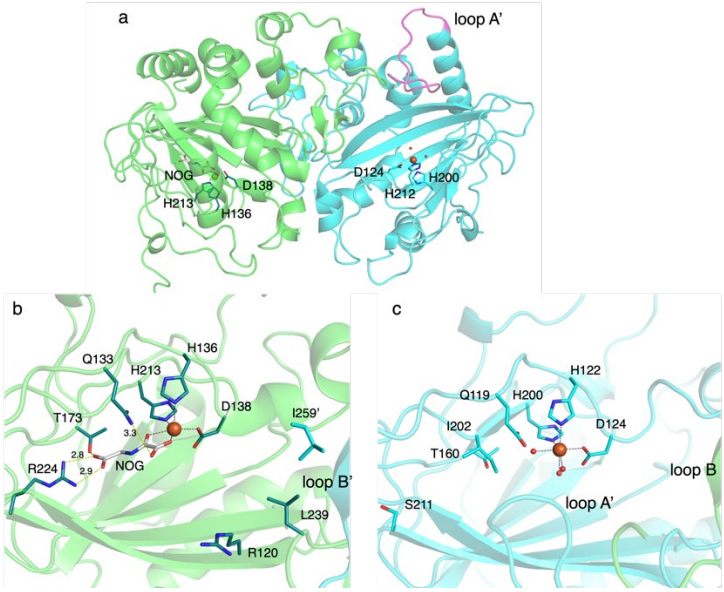

Figure 15. Structure of TlxI-J. (a) The heterodimer structure of TlxI-J-Fe/NOG (PDBID: 7VBQ). The structures of TlxI and TlxJ are colored cyan and green, respectively. The catalytic triad residues and NOG in TlxJ are shown as green and while sticks. The catalytic triad residues in TlxI are shown as cyan sticks. Loop A' is colored magenta. The corresponding loop region in TlxJ is disordered (b and c). Active site structures of TlxJ (green) and TlxI (cyan). Active site residues in TlxJ and TlxI are represented in green and cyan sticks. NOG is shown as white stick. Yellow dashed lines show hydrogen bond interactions. Black dashed lines represent the coordination of the metal atom. The orange spheres show iron atoms. The units of distances are Å. The oxygen and nitrogen atoms are colored red and blue, respectively. Red spheres show water molecules.

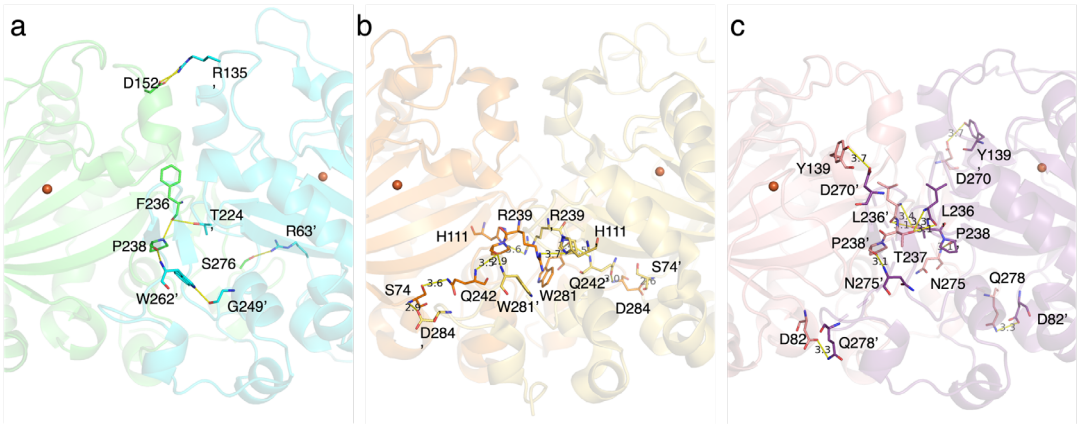

Figure 16. The amino acid residues located at the interface between two monomers of the dimers (a-c) Close-up view of the interface between (a) TlxI and TlxJ heterodimer (PDBID: 7VBQ), (b) the homodimer PrhA (PDBID: 5YBO), and (c) the homodimer AndA (PDBID: 5ZM3). The structures of TlxI and TlxJ are colored cyan and green, those of the PrhA homodimer are orange and yellow, and those of the AndA homodimer are salmon and violet. The amino acid residues which form hydrogen bond interaction are represented as sticks. Hydrogen bond interactions are shown as yellow dashed lines. The orange spheres show iron atoms. The units of distances are Å. The oxygen and nitrogen atoms are colored red and blue, respectively.

6 SptF in Emeridons Biosynthesis

SptF is an αKG OX that reportedly catalyzes two oxidation steps from andiconin D **31** to produce **32** in the biosynthesis of

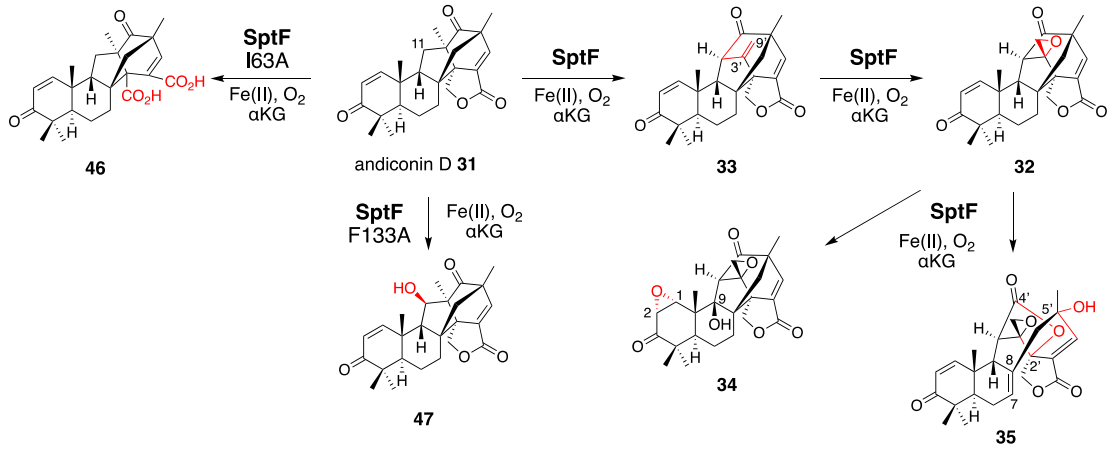

Figure 17. Synthetic reactions from andiconin D 31. The syntheses of 34 and 35 by SptF WT, the synthesis of 46 by SptF I63A, and the synthesis of 47 by SptF F133A.

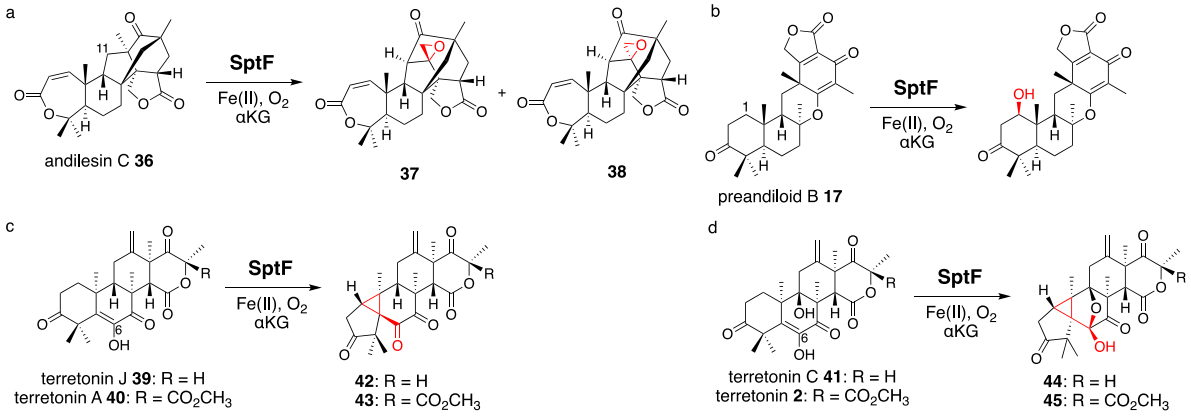

Figure 18. Synthesis of unnatural products by SptF from andilesin C 36 (a), preandiloid B 17 (b), terretonin J 39 and A 40 (c), and terretonin C 41 and terretonin 2 (d).

emeridone F **4**.[51] SptF hydroxylates C-11, followed by water elimination, carbon skeletal rearrangement, and deprotonation to yield **33**, and epoxidizes the C-3'-9' double bond of **33** to yield **32** (Fig. 17). Recent studies revealed that SptF further oxidizes **32** to give two products, **34** with an additional C-9 hydroxyl group and C1-C2 epoxide and **35** with a new ether bridge between C-4' and C-2', a hydroxyl group at C-5', and a double bond between C-7 and C-8.[51] In accordance with the high sequence similarity between SptF and AndF (94%), which is involved in the formation of anditomin **5** from andilesin C **36**,[22] SptF also accepts andilesin C **36** to produce two products **37** and **38**, which possess an epoxide group between C-3' and C-9' with two different absolute configurations, respectively (Fig. 18a).

Inspired by its catalytic versatility, the substrate scope of SptF was further investigated by using six fungal meroterpenoids as unnatural substrates, including preandiloid B **17**, preandiloid C **18**, terretonin J **39**, terretonin A **40**, terretonin C **41**, and terretonin **2** (Fig. 18bcd). Except for **18**, all of the tested substrates were accepted by SptF, indicating that SptF has relaxed substrate specificity. SptF catalyzed the C-1 hydroxylation of **17** (Fig. 18b), and reacted with **39** and **40** to generate **42** and **43** possessing the 5/3/6/6/6 scaffold, and the reaction with **41** and **2** to yield **44** and **45** possessing the 5/3/5/5/6/6 scaffold, respectively (Fig. 18cd). The consumption rates of **40** and **2** by SptF were lower than 10%, indicating that the bulky functional group at the D-ring hampers the reaction. SptF also oxidizes various kinds of steroids, including androsterone, testosterone, and progesterone, with moderate catalytic efficiencies (34-53%).

To determine the molecular basis of the exceptional promiscuity of SptF,[51,52] its X-ray crystallographic structure was analyzed. SptF alone exhibits the conserved DSBH fold (Fig. 19a). The complex structures with **31** and **36** showed that these two substrates are located at almost identical positions, indicating that the A-ring of the substrates does not alter the binding manner. The distances from the iron to the initial reaction site C-11 of **31** and **36** are 4.2 and 4.3 Å, respectively (Fig. 19b and 19c), and are reasonable distances for the hydrogen abstraction. The hydrophobic surface, consisting of I63, F133, and I231, mainly supports the substrate in the enzyme cavity. The lid-like region interacts with the A-rings of **31** and **36** via hydrogen bonding with only N65, while their E rings are supported by S114, the main chain of L199, and T148. The loose interaction with the lid-like Loop explains the broad substrate specificity toward structurally diverse compounds. Interestingly, the unnatural substrate terretonin C **41** was also accepted by SptF in a different ligand binding mode, with the direct hydrogen bond interaction between the D-ring and N150

and the indirect hydrogen bond network via water molecules supported by T148, D130, and L199 (Fig. 19d). Remarkably, the lid-like Loop region was not observed in the complex structure with **41**, while the conformations of the other active site regions are almost identical. In this structure, the substrate is mainly supported by hydrophobic interactions with F133 and I231, which are close to the C-8, C-10, and C-13 methyl groups. The C-6 enol of **41** is closest to the iron (3.7 Å), suggesting that the formations of the cyclopropane rings of **42**, **43**, **44**, and **45** are triggered by the hydrogen bond abstraction from this enol.

To investigate the roles of I63, F133, and I231, they were substituted with alanine. As a result, SptF I63A abolished the production of **34** and **35**, but produced the novel product **46** (Fig. 17). The structure of **46** was determined to be an E-ring opened dicarboxylic acid, which is generated through two rounds of oxidation at the C-1' of **31**. In contrast, the SptF I63A and F133A variants almost completely lost their abilities to produce **34** and **35**, and accumulated **32** and **33**, respectively. The SptF F133A variant also converted **31** into the C-11 hydroxylated **47** (Fig. 17). These data indicated the crucial role of hydrophobic interactions for substrate binding and the potential to engineer the enzyme reaction by site-directed substitutions of the hydrophobic residues.

The importance of the hydrophilic residues, including N65, S114, T148, and N150, was also investigated in detail. N65A significantly reduced the activity by 80% and accumulated **33**. The SptF T148A, S114A, and N150A variants decreased the production efficiencies of **34** and **35** by 7, 17, and 48%, and changed the production ratios of **34**:**35** to 7:3 for the S114A and T148S variants and 1:9 for the N150A variant, as compared with 4:6 for SptF WT. These observations indicated that the three hydrophilic residues are important to define the orientation of **33** within the reaction chamber. When N65 was substituted with threonine, which is the corresponding residue in the closely related AndF, the variant produced **35** as a major product from **31**, with a smaller amount of **34**. In addition to the hydrophobic and hydrophilic interactions, the functions of I63 and N65 in the lid-like Loop region were investigated. Remarkably, the SptF I63A and N65A variants accepted **41** with similar efficiencies to the wild-type enzyme, while the reactivity on **31** was 14 times lower, suggesting the different substrate binding modes between the two substrates. To evaluate the importance of the flexible lid-like Loop region, the Loop was truncated by 6 residues (D6, H61-V66), 9 residues (D9, K58-V66), 16 residues (D16, N54-K69), and 19 residues (W53-K71). The D6, D9, and D16 truncated SptFs were reacted with **31**, **32**, and **33**. Interestingly, these variants lost the activities on **31** and **32**, and generated several minor products, but no longer produced **33**-**35**. In contrast, these variants showed 26-52% activities toward **33**, and generated small amounts of **34** and **35**. This observation suggested that the importance of the lid-like region to control the reaction. While the unnatural meroterpenoid substrates were accepted by the variants to lesser extents, the steroidal substrates were no longer accepted.

Based on the investigations of the structure-function relationships, the reaction mechanisms for the SptF-catalyzed oxidation reactions were proposed (Fig. 20). Hydrogen abstraction at C-11 of **31** by the Fe(IV)=O species firstly generates a radical, which undergoes the cleavage of the C-4'-

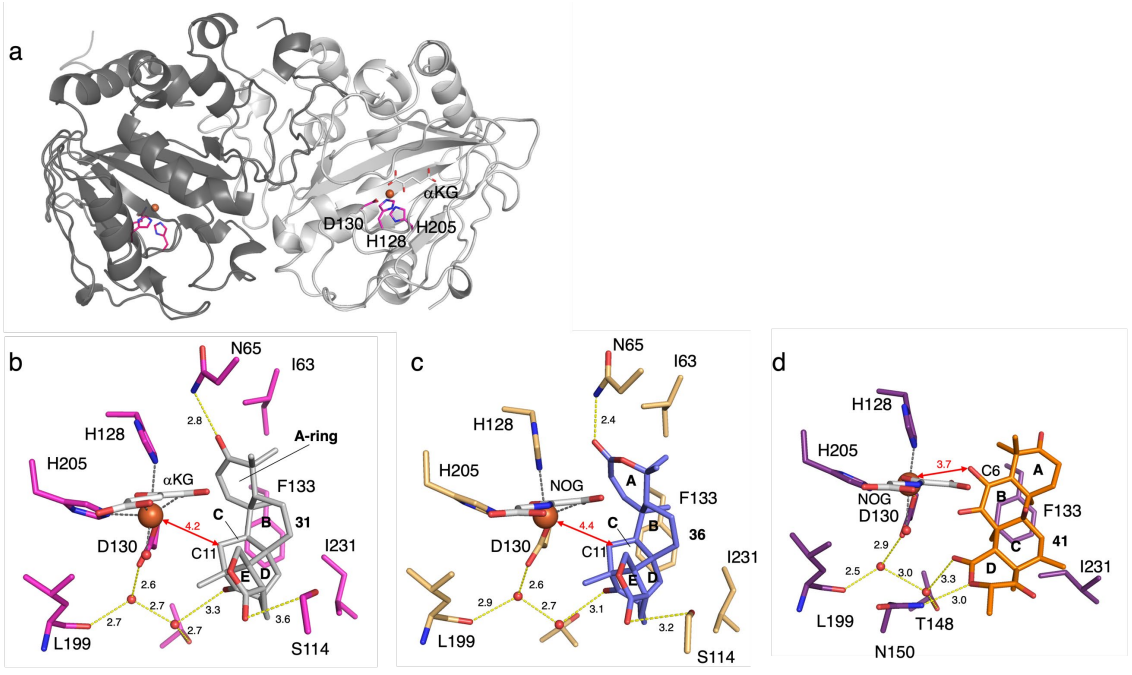

Figure 19. Structure of SptF. (a) The overall structure of SptF (PDBID: 7EYS). The catalytic triad residues are shown in magenta sticks. (b) Active site structures of SptF-Fe/αKG/**31** (PDBID: 7EYS). **31** and αKG are shown as grey and white sticks, respectively. (c) Active site structures of SptF-Fe/NOG/**36** (PDBID: 7EYT). **36** and NOG are shown as blue and white sticks, respectively. (d) Active site structures of SptF-Fe/NOG/**41** (PDBID: 7EYW). **41** and NOG are shown as orange and white sticks, respectively. Yellow dashed lines show hydrogen bond interactions. Black dashed lines represent the metal atom coordination. The iron atom is represented by an orange sphere. The key distances between the iron atom and carbon atoms are shown as arrows. The units of distances are Å. The oxygen and nitrogen atoms are colored red and blue, respectively.

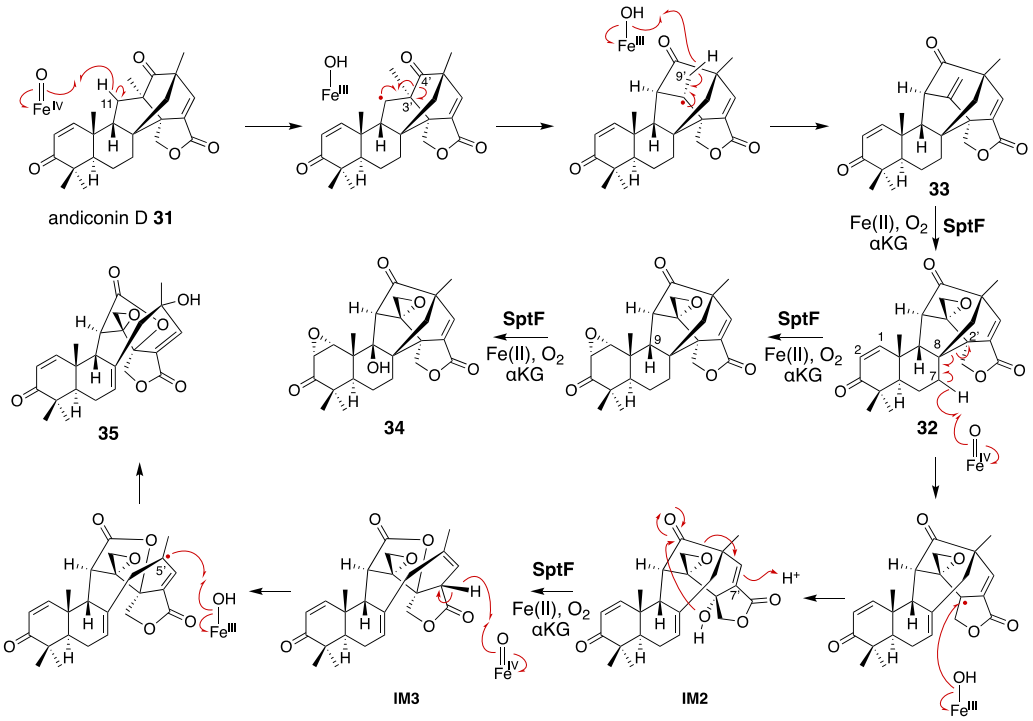

Figure 20. Proposed reaction mechanisms of SptF in the syntheses of 34 and 35 from andiconin D 31.

C-3′ bond and the construction of the C-4′-C-11 bond. The following H-9′ abstraction initiates the formation of the exo-methylene **33**, and the successive epoxidation produces **32**. In pathway a, the second epoxidation of C-1-C-2 and the H-9 abstraction, followed by the rebound of the hydroxyl group, produced **34** as a product. In pathway b, H-7′ is abstracted to induce the cleavage of the C-8-C-2′ bond and generate the double bond between C-7 and C-8. The hydroxyl rebound between the radical at C-2′ and the Fe(III)-hydroxyl species yields IM2. The 2′-OH reacts with the 4′-carbonyl and the subsequent electron migration results in the protonation of C-7′ to generate IM3. The H-7′ in IM3 is abstracted by the Fe(IV)=O species in the next round of oxidation, and the generated allylic radical receives a hydroxyl group at C-5′ from the Fe(III)-OH species to produce **35**.

SptF accepts a remarkably broad range of meroterpenoid and steroid substrates. The solved complex structures revealed the different substrate binding mode for each substrate. Compound **41** can bind to the enzyme in the inverse manner, as compared with those for **31** and **36**. SptF also utilizes the Loop region as a lid for the active site cavity, but it does not appear to bind the substrate tightly. The relaxed binding mode of the Loop region and the hydrophobic reaction chamber would allow the promiscuous substrate binding.

7. Summary and future perspective

In summary, the multifunctional fungal αKG OX enzymes catalyze remarkable chemistries, and often induce dramatic changes in molecular scaffolds, depending on the stereoelectronic character of the substrate/intermediates and the resulting conformational changes/movements of the active site of the enzyme. The X-ray structural analyses of the enzymes revealed which amino acid residues are responsible for the substrate binding as well as the active site architecture to accommodate the bulky terpenoid and polar polyketide moieties. The reaction chambers of αKG OXs are mainly composed of hydrophobic amino acids, which enable the accommodation of the terpene moiety and multiple oxidation reactions (Fig. 21). The structures of the flexible lid-like Loop regions of the active site are significantly different in each enzyme. By manipulating the structures of the reaction chamber and the lid-like Loop regions, their reactions could be modified.

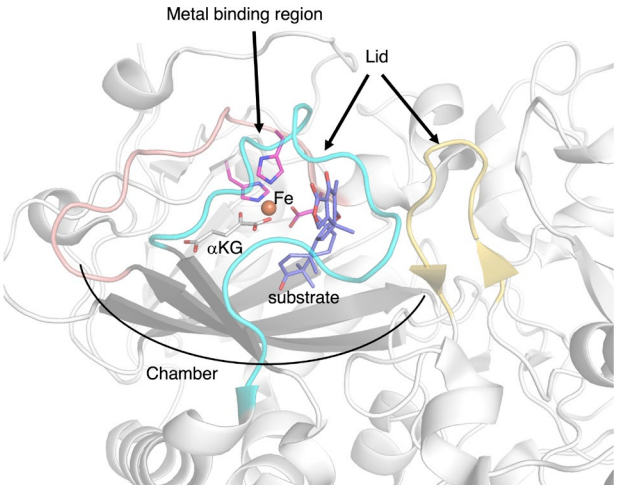

Figure 21. The important structural features of αKG OX enzyme.

To obtain more versatile and useful αKG OX enzymes, further search for new enzymes that catalyze novel reactions or exhibit unique substrate specificities is still needed. The genome mining method would be helpful in searching for such enzymes.[53,54] In the study of the fungal αKG OX AsqJ in the quinolone alkaloid biosynthesis, various research techniques have been applied to elucidate its stepwise desaturation and epoxidation reactions (e.g. X-ray crystallography, pre-steady-state enzyme kinetics, Mössbauer spectroscopy, assays with unnatural substrates, DFT calculations, and molecular dynamic simulations).[29, 55-60] Likewise, studies on structural biology, bioorganic chemistry, and computational chemistry will provide important information for enzyme engineering of αKG OXs. Future development of computational calculations of catalytic reactions is expected to enable highly accurate simulations of enzyme dynamics, which will provide useful insights for more rigorous control of enzyme reactions and creation of biocatalysts by *de novo* design. In addition, a recent engineering study to convert an αKG-dependent amino acid hydroxylase into a halogenase suggested some strategies to evolve the αKG OXs towards enzymes with different catalytic functions.[61] During the writing of this manuscript, two studies based on the saturated random mutagenesis to evolve αKG OXs in meroterpenoid biosynthesis were published.[62,63] Such random mutagenesis-based studies complement the rational enzyme engineering. Finally, the engineered enzymes can be utilized in combinatorial biosyntheses in heterologous expression hosts such as *Aspergillus oryzae*, to produce pharmaceutically useful molecules, as demonstrated by the recent successful productions of unnatural novel diterpene fungal meroterpenoids.[64-66] Therefore, the discovery, engineering, and reconstitution of fungal meroterpenoid oxidation pathway will continue to provide important insights into natural product chemistry and enzymology, and will lead to the production of beneficial drug seeds.

8. Conflicts of interest

There are no conflicts to declare.

9. Acknowledgements

The authors would like to express sincere appreciation to an excellent group of coworkers whose contributions are cited in the text, in particular to Dr. Yudai Matsuda (City University of Hong Kong). This work was supported in part by a Grant-in-Aid for Scientific Research from the Ministry of Education, Culture, Sports, Science and Technology, Japan (JSPS KAKENHI Grant Number JP16H06443, JP17H04763, JP18K19139, JP19H04641, JP19K15703, JP20H00490, JP20KK0173, JP20K22700, JP21H02636, JP21K14744, and JP21K18246), the New Energy and Industrial Technology Development Organization (NEDO, Grant Number JPNP20011), AMED (Grant Number JP21ak0101164), UTEC-UTokyo FSI Research Grant Program, the PRESTO and ACT-X Programs from Japan Science and Technology Agency, Fuji Foundation for Protein Research, Japan Foundation for Applied Enzymology, Kato Memorial Bioscience Foundation, The Asahi Glass Foundation, and Naito foundation.

10. Notes and references

1 R. Geris and T. J. Simpson, *Nat. Prod. Rep.*, 2009, **26**, 1063–1094.
2 Y. Matsuda and I. Abe, *Nat. Prod. Rep.*, 2016, **33**, 26–53.
3 Y. Matsuda, T. Awakawa, T. Mori and I. Abe, *Curr. Opin. Chem. Biol.*, 2016, **31**, 1–7.
4 T. Awakawa and I. Abe, *J. Fungi*, 2021, **7**, 486.
5 H. Tao and I. Abe, *Curr. Opin. Biotechnol.*, 2021, **69**, 52–59.
6 L. Barra and I. Abe, *Nat. Prod. Rep.*, 2021, **38**, 566–585.
7 X. Zhang, J. Guo, F. Chenga and S. Li, *Nat. Prod. Rep.*, 2021, **38**, 1072–1099.
8 H. Nakamura, Y. Matsuda and I. Abe, *Nat. Prod. Rep.*, 2018, **35**, 633–645.
9 M. C. Tang, Y. Zou, K. Watanabe, C. T. Walsh and Y. Tang, *Chem. Rev.*, 2017, **117**, 5226–5333.
10 R. Cox, *Nat. Prod. Rep.*, 2014, **31**, 1405–1424.
11 T. Mori, T. Iwabuchi, S. Hoshino, H. Wang, Y. Matsuda and I. Abe, *Nat. Chem. Biol.*, 2017, **13**, 1066–1073.
12 W. Aik, M. A. McDonough, A. Thalhammer, R. Chowdhury and C. J. Schofield, *Curr. Opin. Struct. Biol.*, 2012, **22**, 691–700.
13 S. Islam, T. M. Leissing, R. Chowdhury, R. J. Hopkinson and C. J. Schofield, *Annu. Rev. Biochem.*, 2018, **87**, 585–620.
14 S. S. Gao, N. Naowarojna, R. Cheng, X. Liu and P. Liu, *Nat. Prod. Rep.*, 2018, **35**, 792–837.
15 C. R. Zwick and H. Renata, *Nat. Prod. Rep.*, 2020, **37**, 1065–1079.
16 I. Abe, *Chem. Pharm. Bull.*, 2020, **68**, 823–831.
17 L. F. Wu, S. Meng and G. L. Tang, *Biochim. Biophys. Acta - Proteins Proteomics*, 2016, **1864**, 453–470.
18 X. Huang and J. T. Groves, *J. Biol. Inorg. Chem.*, 2017, **22**, 185–207.
19 C. Krebs, D. Galonić Fujimori, C. T. Walsh and J. M. B. Jr, *Acc. Chem. Res.*, 2007, **40**, 484–492.
20 J. Li, H. J. Liao, Y. Tang, J. L. Huang, L. Cha, T. S. Lin, J. L. Lee, I. V. Kurnikov, M. G. Kurnikova, W. C. Chang, N. L. Chan and Y. Guo, *J. Am. Chem. Soc.*, 2020, **142**, 6268–6284.
21 R. Bunno, T. Awakawa, T. Mori and I. Abe, *Angew. Chemie - Int. Ed.*, 2021, **60**, 15827–15831.
22 Y. Matsuda, T. Awakawa, T. Wakimoto and I. Abe, *J. Am. Chem. Soc.*, 2013, **135**, 10962–10965.
23 Y. Matsuda, T. Iwabuchi, T. Fujimoto, T. Awakawa, Y. Nakashima, T. Mori, H. Zhang, F. Hayashi and I. Abe, *J. Am. Chem. Soc.*, 2016, **138**, 12671–12677.
24 Y. Nakashima, T. Mori, H. Nakamura, T. Awakawa, S. Hoshino, M. Senda, T. Senda and I. Abe, *Nat. Commun.*, 2018, **9**, Article number: 104.
25 P. Schrepfer, A. Buettner, C. Goerner, M. Hertel, J. Van Rijn, F. Wallrapp, W. Eisenreich, V. Sieber, R. Kourist and T. Brück, *Proc. Natl. Acad. Sci. U. S. A.*, 2016, **113**, E958–E967.
26 H. Sato, K. Narita, A. Minami, M. Yamazaki, C. Wang, H. Suemune, S. Nagano, T. Tomita, H. Oikawa and M. Uchiyama, *Sci. Rep.*, 2018, **8**, 1–9.
27 Y. Matsuda, T. Wakimoto, T. Mori, T. Awakawa and I. Abe, *J. Am. Chem. Soc.*,2014, **136**, 15326–15336.
28 Y. Nakashima, T. Mitsuhashi, Y. Matsuda, M. Senda, H. Sato, M. Yamazaki, M. Uchiyama, T. Senda and I. Abe, *J. Am. Chem. Soc.*, 2018, **140**, 9743–9750.
29 H. J. Liao, J. Li, J. L. Huang, M. Davidson, I. Kurnikov, T. S. Lin, J. L. Lee, M. Kurnikova, Y. Guo, N. L. Chan and W. C. Chang, *Angew. Chemie - Int. Ed.*,2018, **57**, 1831–1835.
30 W. Yan, H. Song, F. Song, Y. Guo, C. H. Wu, A. Sae Her, Y. Pu, S. Wang, N. Naowarojna, A. Weitz, M. P. Hendrich, C. E.

Costello, L. Zhang, P. Liu and Y. Jessie Zhang, *Nature*, 2015, **527**, 539–543. This paper was retracted on 27 May 2021.
31 N. P. Dunham, J. M. Del Río Pantoja, B. Zhang, L. J. Rajakovich, B. D. Allen, C. Krebs, A. K. Boal and J. M. Bollinger, *J. Am. Chem. Soc.*, 2019, **141**, 9964–9979.
32 L. Wu, Z. Wang, Y. Cen, B. Wang and J. Zhou, *Angew. Chemie - Int. Ed.*, 2022, **134**, e202112063.
33 W. C. Chang, Y. Guo, C. Wang, S. E. Butch, A. C. Rosenzweig, A. K. Boal, C. Krebs and J. M. Bollinger, *Science*, 2014, **343**, 1140–1144.
34 V. Siitonen, B. Selvaraj, L. Niiranen, Y. Lindqvist, G. Schneider and M. Metsä-Ketelä, *Proc. Natl. Acad. Sci. U. S. A.*, 2016, **113**, 5251–5256.
35 Y. Matsuda, T. Bai, C. B. W. Phippen, C. S. Nødvig, I. Kjærbølling, T. C. Vesth, M. R. Andersen, U. H. Mortensen, C. H. Gotfredsen, I. Abe and T. O. Larsen, *Nat. Commun.*, 2018, **9**, Article number: 2587.
36 T. Mori, R. Zhai, R. Ushimaru, Y. Matsuda and I. Abe, *Nat. Commun.*, 2021, **12**, Article number: 4417.
37 V. J. Chen, A. M. Orville, M. R. Harpel, C. A. Frolik, K. K. Surerus, E. Munck and J. D. Lipscomb, *J. Biol. Chem.*, 1989, **264**, 21677–21681.
38 J. E. Dotzlaf and W. K. Yeh, *J. Biol. Chem.*, 1989, **264**, 10219–10227.
39 W. A. Van der Donk, A. L. Tsai and R. J. Kulmacz, *Biochemistry*, 2002, **41**, 15451–15458.
40 J. Pan, E. S. Wenger, M. L. Matthews, C. J. Pollock, M. Bhardwaj, A. J. Kim, B. D. Allen, R. B. Grossman, C. Krebs and J. Martin Bollinger, *J. Am. Chem. Soc.*, 2019, **141**, 15153–15165.
41 X. Cao, Y. Shi, X. Wu, K. Wang, S. Huang, H. Sun, J. S. Dickschat and B. Wu, *Org. Lett.*, 2019, **21**, 6539–6542.
42 X. Cao, Y. Shi, S. Wu, X. Wu, K. Wang, H. Sun, S. He, J. S. Dickschat and B. Wu, *Tetrahedron*, 2020, **76**, 131349.
43 X. Li, T. Awakawa, T. Mori, M. Ling, D. Hu, B. Wu and I. Abe, *J. Am. Chem. Soc.*, 2021, **143**, 21425–21432.
44 C. C. Liaw, Y. L. Yang, C. K. Lin, J. C. Lee, W. Y. Liao, C. N. Shen, J. H. Sheuand S. H. Wu, *Org. Lett.*, 2015, **17**, 2330–2333.
45 W. D. Nes, *Chem. Rev.*, 2011, **111**, 6423–6451.
46 J. M. Lv, D. Hu, H. Gao, T. Kushiro, T. Awakawa, G. D. Chen, C. X. Wang, I. Abe and X. S. Yao, *Nat. Commun.* 2017, **8**, Article number: 1644.
47 C. F. Lee, L. X. Chen, C. Y. Chiang, C. Y. Lai and H. C. Lin, *Angew. Chemie - Int. Ed.*, 2019, **58**, 18414–18418.
48 O. W. Choroba, D. H. Williams and J. B. Spencer, *J. Am. Chem. Soc.*, 2000, **122**, 5389–5390.
49 B. K. Hubbard, M. G. Thomas and C. T. Walsh, *Chem. Biol.*, 2000, **7**, 931–942.
50 E. Kalliri, P. K. Grzyska and R. P. Hausinger, *Biochem. Biophys. Res. Commun.*,2005, **338**, 191–197.
51 T. Bai, Y. Matsuda, H. Tao, T. Mori, T. Mori, Y. Zhang and I. Abe, *Org. Lett.*, 2020, **22**, 4311–4315.
52 H. Tao, T. Mori, H. Chen, S. Lyu, A. Nonoyama, S. Lee and I. Abe, *Nat. Commun.*, 2022, **13**, Article number: 95.
53 D. Yan and Y. Matsuda, *Org. Lett.*, 2021, **23**, 3211–3215.
54 J. Davison, A. Al Fahad, M. Cai, Z. Song, S. Y. Yehia, C. M. Lazarus, A. M. Bailey, T. J. Simpson and R. J. Cox, *Proc. Natl. Acad. Sci. U. S. A.*, 2012, **109**, 7642–7647.
55 N. Ishikawa, H. Tanaka, F. Koyama, H. Noguchi, C. C. C. Wang, K. Hotta and K. Watanabe, *Angew. Chemie - Int. Ed.*, 2014, **53**, 12880–12884.
56 W. C. Chang, J. Li, J. L. Lee, A. A. Cronican and Y. Guo, *J. Am. Chem. Soc.*, 2016, **138**, 10390–10393.
57 X. Song, J. Lu and W. Lai, *Phys. Chem. Chem. Phys.*, 2017, **19**, 20188–20197.
58 S. L. Mader, A. Bräuer, M. Groll and V. R. I. Kaila, *Nat. Commun.*, 2018, **9**, 1–8.
59 J. Pan, E. S. Wenger, M. L. Matthews, C. J. Pollock, M. Bhardwaj, A. J. Kim, B. D. Allen, R. B. Grossman, C. Krebs and J. Martin Bollinger, *J. Am. Chem. Soc.*, 2019, **141**, 15153–15165.
60 J. Li, H. J. Liao, Y. Tang, J. L. Huang, L. Cha, T. S. Lin, J. L. Lee, I. V. Kurnikov, M. G. Kurnikova, W. C. Chang, N. L. Chan and Y. Guo, *J. Am. Chem. Soc.*, 2020, **142**, 6268–6284.
61 M. E. Neugebauer, E. N. Kissman, J. A. Marchand, J. G. Pelton, N. A. Sambold, D. C. Millar and M. C. Y. Chang, *Nat. Chem. Biol.*, 2022, **18**, 171–179.
62 T. Mori, Y. Nakashima, H. Chen, S. Hoshino, T. Mitsuhashi and I. Abe, *Chem. Commun.*, 2022, **58**, 5510–5513.
63 T. Mori, Z. Yu, H. Tao and I. Abe, *Org. Lett.*, 2022, **24**, 1737–1741.
64 K. Tsukada, S. Shinki, A. Kaneko, K. Murakami, K. Irie, M. Murai, H. Miyoshi, S. Dan, K. Kawaji, H. Hayashi, E. N. Kodama, A. Hori, E. Salim, T. Kuraishi, N. Hirata, Y. Kanda and T. Asai, *Nat. Commun.*, 2020, **11**, Article number: 1830.
65 Y. Morishita, K. Tsukada, K. Murakami, K. Irie and T. Asai, *J. Nat. Prod.*, 2022, **85**, 384–390.
66 Z.-H. Xiao, J.-Y. Dong, A. Li, J.-M. Dai, Y.-P. Li, Q.-F. Hu, L.-D. Shao, Y. Matsuda and W.-G. Wang, *Org. Chem. Front.*, 2022, **9**, 1837–1843.